POLITECNICO DI TORINO
Repository ISTITUZIONALE

Wavelet-Based High-Order Adaptive Modeling of Lossy Interconnects

Original
Wavelet-Based High-Order Adaptive Modeling of Lossy Interconnects / GRIVET TALOCIA, Stefano; Canavero, Flavio. - In: IEEE TRANSACTIONS ON ELECTROMAGNETIC COMPATIBILITY. - ISSN 0018-9375. - STAMPA. - 43:4(2001), pp. 471-484. [10.1109/15.974626]

Availability:
This version is available at: 11583/1401327 since:

Publisher:
IEEE

Published
DOI:10.1109/15.974626

Terms of use:

This article is made available under terms and conditions as specified in the corresponding bibliographic description in the repository

Publisher copyright

(Article begins on next page)

25 April 2024

Wavelet-Based High-Order Adaptive Modeling of Lossy Interconnects

S. Grivet-Talocia and F. Canavero

***Abstract*—This paper presents a numerical-modeling strategy for simulation of fast transients in lossy electrical interconnects. The proposed algorithm makes use of wavelet representations of voltages and currents along the structure, with the aim of reducing the computational complexity of standard time-domain solvers. A special weak procedure for the implementation of possibly dynamic and nonlinear boundary conditions allows to preserve stability as well as a high approximation order, thus leading to very accurate schemes. On the other hand, the wavelet expansion allows the computation of the solution by using few significant coefficients which are automatically determined at each time step. A dynamically refinable mesh is then used to perform a sparse time-stepping. Several numerical results illustrate the high efficiency of the proposed algorithm, which has been tuned and optimized for best performance in fast digital applications typically found on modern PCB structures.**

***Index Terms*—Finite difference methods, time-domain analysis, transmission lines, wavelet transforms.**

I. Introduction

THE ever-increasing demand for faster and faster digital applications is leading to a great effort of both academia and industry for the development of new analysis and design tools for printed circuit board (PCB) structures. These tools should provide precise and complete characterizations, with special attention to all the possible causes of signal degradation which inevitably leads to malfunctioning. These causes include losses, crosstalk, nonuniformity, and interference from external fields. It is well-known that electrical interconnects are one of the most sensitive parts of modern PCB structures to these effects. We then study in this paper the transient behavior of electrical interconnects by means of a new wavelet-based adaptive algorithm.

We concentrate in this paper on interconnects that can be modeled through the multiconductor transmission lines (MTL) equations. Therefore, we will assume without further check that the fields surrounding the structure have a dominant transverse component (quasi-TEM modes), even in the presence of high losses, dielectric discontinuities, and longitudinal non uniformities [22], [11]. The quasi-TEM assumption holds in many cases of practical interest.

The numerical modeling of electrical interconnects can be performed with some standard schemes in both frequency domain and time domain. We focus here on time-domain modeling since frequency-domain does not allow inclusion of nonlinear terminations, which are commonly found in practical situations and which play a crucial role under the signal integrity standpoint. Due to its simplicity, the finite-difference time-domain (FDTD) scheme [17], [29] is usually employed for time-domain simulation. This method allows the inclusion of nonlinear and dynamic terminations [20] and skin effect losses [25], but its accuracy is limited to second order. This implies a high number of unknowns for electrically long interconnects.

We present in this paper a discretization strategy based on high-order finite differences. These allow a significant reduction of the most relevant sources of numerical errors for FDTD, namely numerical dispersion [13], [14], thus allowing use of a reduced number of unknowns for the computation of the solution at a prescribed accuracy. However, high-order schemes present some difficulties in the treatment of the boundary conditions. Indeed, preservation of high order at all spatial nodes may lead to late time instability [1], [2], [27], [28]. For this reason, we present a novel procedure based on a weak approximation of the boundary equations, which preserves strict stability of the terminated scheme even with high-order differences at the boundary nodes. The implementation is straightforward. The final outcome is a modeling tool for arbitrary interconnects (including the case of frequency-dependent losses) terminated by arbitrary nonlinear and dynamic loads. It should be noted that behavioral models of actual digital ports [18] may also be included in such framework.

The main result of this paper is the optimization of the above-mentioned high-order discretization through wavelet-based adaptive strategies. Indeed, a typical transient waveform traveling on PCB interconnects presents some smooth regions (well-treated by high-order schemes) and localized regions with faster variations (like, e.g., steep fronts of digital pulses). The latter require in any case a high density of discretization nodes to insure accurate representations. However, a very fine discretization is not required in the smooth regions. It is then natural to resort to some more advanced representation allowing mesh coarsening and refinement on the basis of the structure of the solution. Wavelets are the most appropriate mathematical tool to be employed in such cases [9], [10], [15]. We will show how a simple change of basis in the representation of the solution allows to work with wavelet coefficients instead of nodal values. Most of these coefficients can be neglected without significantly affecting the accuracy of the simulation, leading to highly sparse representations. The number of operations required for the simulation are then significantly reduced with respect to nonadaptive schemes.

The paper is organized as follows. Section II details the problem under investigation and the equations that will be

Manuscript received July 30, 2000; revised March 31, 2001.

The authors are with the Dipartimento di Elettronica, Politecnico di Torino, Turin 10129, Italy (e-mail: grivet@polito.it).

Publisher Item Identifier S 0018-9375(01)10226-7.

0018–9375/01$10.00 © 2001 IEEE

solved numerically. Section III describes the high-order difference approximations together with the stable implementation of the termination equations. Also the treatment of skin effect losses and the choice of time discretization are detailed here. Section IV describes the wavelet-based adaptive approximation, the criteria leading to a sparse representation of the solution, and the main algorithm exploiting dynamic mesh refinement and coarsening. Section V illustrates the efficiency of the proposed scheme through a set of numerical examples. Finally, conclusions are drawn in Section VI.

II. Problem Statement

The structure under investigation is an electrical interconnect made of an arbitrary number M of conductors (plus reference) and described by the MTL equations [22]

$$\frac{\partial}{\partial z}\mathbf{v}(z,t)+\mathbf{L}\frac{\partial}{\partial t}\mathbf{i}(z,t)+\mathbf{Z}_i(t)*\mathbf{i}(z,t)=0 \tag{1}$$

$$\frac{\partial}{\partial z}\mathbf{i}(z,t)+\mathbf{C}\frac{\partial}{\partial t}\mathbf{v}(z,t)+\mathbf{G}\mathbf{v}(z,t)=0 \tag{2}$$

where boldface quantities are used to indicate vectors or matrices. The line geometry is taken into account in the definition of the per-unit-length inductance $\mathbf{L}$, capacitance $\mathbf{C}$, and conductance $\mathbf{G}$ matrices. The conductor losses are represented by the transient internal impedance matrix $\mathbf{Z}_i(t)$, which is defined in the Laplace domain as

$$\mathbf{Z}_i(t)\Leftrightarrow\mathbf{Z}_i(s)=\mathbf{R}(s)+s\mathbf{L}_i(s)$$

where $\mathbf{R}(s)$ is the per-unit-length resistance and $\mathbf{L}_i(s)$ the per-unit-length internal inductance related to the magnetic flux within the conductors. The frequency-dependent losses due to skin effect are herewith approximated through the commonly used Holt model [19]

$$\mathbf{Z}_i(s)\simeq\mathbf{A}+\mathbf{B}\sqrt{s}$$

which inserted into the MTL equations gives rise to a time-domain convolution term [22], [25]

$$\frac{\partial}{\partial z}\mathbf{v}(z,t)+\mathbf{L}\frac{\partial}{\partial t}\mathbf{i}(z,t)+\mathbf{A}\mathbf{i}(z,t)+\mathbf{B}\frac{1}{\sqrt{\pi t}}*\frac{\partial}{\partial t}\mathbf{i}(z,t)=0 \tag{3}$$

$$\frac{\partial}{\partial z}\mathbf{i}(z,t)+\mathbf{C}\frac{\partial}{\partial t}\mathbf{v}(z,t)+\mathbf{G}\mathbf{v}(z,t)=0. \tag{4}$$

This is a classical model for skin-effect losses, which has been extensively used in the related literature. On the other hand, it is well-known that this model may be too idealized for the representation of more complicated frequency dependent parameters in modern technologies. However, the numerical scheme employed in this work, which is based on the Prony's approximation [21], may be applied in principle to other skin-effect models. Therefore, we will only consider the Holt model in the following, noting that other models could be accounted for by re-computing the Prony coefficients of Table I according to the procedure detailed in Section III.

TABLE I
Coefficients of the Prony Approximation of Z_0^*

i	a_i	b_i
1	6.5136923e-02	-7.5470580e-04
2	1.0881144e-01	-1.0325554e-02
3	1.1439146e-01	-4.3209494e-02
4	2.3975029e-01	-1.1682521e-01
5	-4.4833289e-02	-2.5022317e-01
6	9.0501190e-01	-4.6685236e-01
7	-1.4431210e+00	-8.0124601e-01
8	4.0778027e+00	-1.3163285e+00
9	-6.9208923e+00	-2.1629783e+00
10	1.8611191e+01	-3.9532452e+00

It will be convenient to express (3)–(4) in a time-explicit form. Therefore, we premultiply the MTL equations by $\mathbf{\Gamma}=\mathbf{L}^{-1}$ and $\mathbf{S}=\mathbf{C}^{-1}$, respectively, obtaining

$$\frac{\partial}{\partial t}\mathbf{i}(z,t)=-\mathbf{\Gamma}\frac{\partial}{\partial z}\mathbf{v}(z,t)-\mathbf{\Gamma}\mathbf{A}\mathbf{i}(z,t)-\mathbf{\Gamma}\mathbf{B}\frac{1}{\sqrt{\pi t}}*\frac{\partial}{\partial t}\mathbf{i}(z,t) \tag{5}$$

$$\frac{\partial}{\partial t}\mathbf{v}(z,t)=-\mathbf{S}\frac{\partial}{\partial z}\mathbf{i}(z,t)-\mathbf{S}\mathbf{G}\mathbf{v}(z,t). \tag{6}$$

The discretization described in Section III requires the solution to be expressed in terms of forward and backward propagating waves for proving strict late time stability. For this reason, we apply the modal transformation in order to decouple the above system. We define the frequency-independent modal transformation matrix $\mathbf{T}$ such that the product $\mathbf{T}^{-1}\mathbf{S}\mathbf{\Gamma}\mathbf{T}$ is diagonal. Introducing the modal voltages and currents through

$$\mathbf{v}(z,t)=\mathbf{T}\mathbf{v}^m(z,t),\quad \mathbf{i}(z,t)=\mathbf{T}^{-T}\mathbf{i}^m(z,t)$$

where the superscript $^{-T}$ indicates inverse and transpose, we get

$$\frac{\partial}{\partial t}\mathbf{i}^m(z,t)=-\mathbf{g}\frac{\partial}{\partial z}\mathbf{v}^m(z,t)-\mathbf{T}^T\mathbf{\Gamma}\mathbf{A}\mathbf{T}^{-T}\mathbf{i}^m(z,t)-\mathbf{T}^T\mathbf{\Gamma}\mathbf{B}\mathbf{T}^{-T}\frac{1}{\sqrt{\pi t}}*\frac{\partial}{\partial t}\mathbf{i}^m(z,t) \tag{7}$$

$$\frac{\partial}{\partial t}\mathbf{v}^m(z,t)=-\mathbf{s}\frac{\partial}{\partial z}\mathbf{i}^m(z,t)-\mathbf{T}^{-1}\mathbf{S}\mathbf{G}\mathbf{T}\mathbf{v}^m(z,t) \tag{8}$$

where $\mathbf{s}=\mathbf{T}^{-1}\mathbf{S}\mathbf{T}^{-T}$ and $\mathbf{g}=\mathbf{T}^T\mathbf{\Gamma}\mathbf{T}$ are diagonal. Note that only the lossless part of the MTL equations is diagonalized, since the matrices related to losses are in general full. It is indeed well known that a frequency-independent modal decomposition does not allow full decoupling [23]. The voltages and currents are decomposed into the different modes characteristic of the lossless part of the MTL. With a slight abuse of language we will consistently denote these as "modes" throughout the paper. However, it should be kept in mind that "cross-modal" coupling exists through losses.

Defining the modal (diagonal) characteristic impedance $\mathbf{z}$ and velocity $\mathbf{c}$ matrices as

$$\mathbf{z}=\mathbf{s}^{1/2}\mathbf{g}^{-1/2}=\mathbf{g}^{-1/2}\mathbf{s}^{1/2},\quad \mathbf{c}=\mathbf{s}^{1/2}\mathbf{g}^{1/2}=\mathbf{g}^{1/2}\mathbf{s}^{1/2}$$

and defining the forward and backward power waves $\mathbf{a}(z,t)$, $\mathbf{b}(z,t)$ through

$$\begin{bmatrix} \mathbf{i}^m(z,t) \\ \mathbf{v}^m(z,t) \end{bmatrix} = \mathbf{X} \begin{bmatrix} \mathbf{a}(z,t) \\ \mathbf{b}(z,t) \end{bmatrix}, \quad \mathbf{X} = \begin{bmatrix} \mathbf{z}^{-1/2} & -\mathbf{z}^{-1/2} \\ \mathbf{z}^{1/2} & \mathbf{z}^{1/2} \end{bmatrix}$$

we get the final form of the MTL equations

$$\frac{\partial}{\partial t} \begin{bmatrix} \mathbf{a}(z,t) \\ \mathbf{b}(z,t) \end{bmatrix} = -\begin{bmatrix} \mathbf{c} & 0 \\ 0 & -\mathbf{c} \end{bmatrix} \frac{\partial}{\partial z} \begin{bmatrix} \mathbf{a}(z,t) \\ \mathbf{b}(z,t) \end{bmatrix} - \mathbf{K}_1 \begin{bmatrix} \mathbf{a}(z,t) \\ \mathbf{b}(z,t) \end{bmatrix} - \mathbf{K}_2 \frac{1}{\sqrt{\pi t}} * \frac{\partial}{\partial t} \begin{bmatrix} \mathbf{a}(z,t) \\ \mathbf{b}(z,t) \end{bmatrix} \quad (9)$$

where

$$\mathbf{K}_1 = \mathbf{X}^{-1} \begin{bmatrix} \mathbf{T}^T \mathbf{\Gamma} \mathbf{A} \mathbf{T}^{-T} & 0 \\ 0 & \mathbf{T}^{-1} \mathbf{S} \mathbf{G} \mathbf{T} \end{bmatrix} \mathbf{X},$$
$$\mathbf{K}_2 = \mathbf{X}^{-1} \begin{bmatrix} \mathbf{T}^T \mathbf{\Gamma} \mathbf{B} \mathbf{T}^{-T} & 0 \\ 0 & 0 \end{bmatrix} \mathbf{X}.$$

It should be noted that the above-defined power waves coincide with scattering waves defined with a reference impedance equal to the characteristic impedance $\mathbf{Z}_C = \mathbf{T}\mathbf{z}\mathbf{T}^T$ of the lossless part of the MTL.

The terminations that will be considered in this work are arbitrary nonlinear and dynamic networks, in order to model all kinds of lumped ports that can be found on PCBs. We can express the terminations dynamics through, e.g., their state equations. If we define the array $\mathbf{x}$ collecting all the internal states of any termination (i.e., capacitor voltages and inductor currents), we can write

$$\begin{cases} \mathbf{H} \frac{d}{dt} \mathbf{x}(t) = \mathcal{F}(\mathbf{x}(t), \mathbf{w}_{\text{inc}}(t), \mathbf{u}(t)) \\ \mathbf{w}_{\text{ref}}(t) = \mathcal{G}(\mathbf{x}(t), \mathbf{w}_{\text{inc}}(t), \mathbf{u}(t)) \end{cases} \quad (10)$$

where $\mathbf{H}$ is a symmetric strictly positive definite matrix collecting the lumped capacitances and (possibly coupled) inductances of the termination, and $\mathbf{w}_{\text{inc}}$, $\mathbf{w}_{\text{ref}}$ indicate, respectively, the incident and reflected power waves (scattering waves defined as above) at the termination. The above expression has some advantages with respect to more standard forms using voltages and currents. First, since the scattering waves propagate along the MTL almost independently (they are coupled only through losses), the incident waves into the terminations depend (almost) only on the electrical state of the MTL and not of the termination. These must be regarded as "causes" exciting the termination dynamics and the state $\mathbf{x}(t)$. The time evolution of the state must not depend on the reflected waves, since they would propagate away from the termination. These must be regarded as "effects" induced by the incident waves and by the termination dynamics. Hence, the reflected waves appear only in the output section of the state equations. Second, the above expressions will allow to prove rigorously the strict stability of the terminated scheme to be presented in Section III.

The simple equivalent circuits of Fig. 1 may be used to write down the termination equations in the form of (10). The MTL section is replaced by a vector Thévénin or Norton equivalent circuit with internal impedance equal to $\mathbf{Z}_C$. The equivalent voltage or current sources are proportional to the incident wave vector $\mathbf{w}_{\text{inc}}$ through

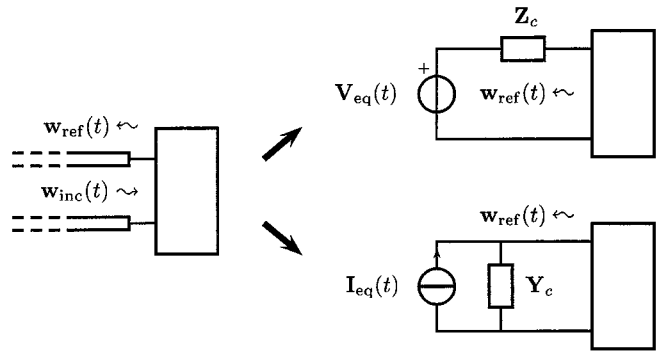

Fig. 1. Equivalent circuit for the derivation of the state equations for the termination networks. The equivalent voltage and current sources are related to the incident wave vector through (11), while $\mathbf{Y}_c = \mathbf{Z}_c^{-1}$.

$$\mathbf{V}_{\text{eq}}(t) = 2\mathbf{T}\mathbf{z}^{1/2}\mathbf{w}_{\text{inc}}(t), \quad \mathbf{I}_{\text{eq}}(t) = 2\mathbf{T}^{-T}\mathbf{z}^{-1/2}\mathbf{w}_{\text{inc}}(t). \quad (11)$$

Both circuits are formally equivalent. However, the Norton circuit may be more suitable for direct implementation of the transmission-line segments into some standard circuit simulation environment based on modified nodal analysis (MNA) [26], [31]. It should be noted that in the simple case of passive linear static terminations the size of the state vector reduces to zero, and the usual expressions relating the reflected waves to the incident waves through the scattering matrix or reflection coefficient matrix are recovered.

III. High-Order Approximation of MTL Equations

The discretization of the MTL equations (9) is performed through three separate steps. First, the line is subdivided into $N+1$ evenly spaced nodes $\{z_i = i\Delta z, i = 0, \ldots, N\}$ and a suitable spatial difference approximation is performed. Then, the boundary equations are inserted. Finally, a time discretization is applied in order to get a time-stepping scheme. In this last stage also the convolution terms due to skin effect losses are treated.

We begin with the spatial approximation, which is performed through a suitable finite difference operator of arbitrary order τ. In general, given the arrays $\mathbf{f}$ collecting the $N+1$ nodal values f_i of any function $f(z)$, and $\mathbf{f}_z$ collecting the nodal values of its first derivative, the scheme can be cast in the general form

$$\mathbf{f}_z = \mathbf{P}^{-1}\mathbf{Q}\mathbf{f} + \mathbf{e}, \quad \|\mathbf{e}\| = O(\Delta z^\tau)$$

where Δz is the spatial grid size. Note that we are including in this formulation, also implicit differentiation schemes due to the presence of matrix $\mathbf{P}$. Both matrices $\mathbf{P}$ and $\mathbf{Q}$ are generally banded with few nonvanishing diagonals, the number of entries per row being related to the order τ of the scheme. This abstract formulation takes into account the nonsymmetric differentiation stencils related to the nodes close to the edges of the domain.

We will constrain our analysis only to those difference approximations satisfying certain symmetry conditions, which are

indeed essential to prove strict stability of the boundary treatment [2], [27]. Specifically,

$$\mathbf{P} = \mathbf{P}^T, \quad \mathbf{P} > 0, \quad \mathbf{f}^T(\mathbf{Q} + \mathbf{Q}^T)\mathbf{f} = 2q_0 f_0^2 + 2q_N f_N^2$$

with $q_0 < 0 < q_N$. These are called Summation-By-Parts (SBP) operators [27], [28]. When applied to . (9), we get the following expression,

$$\begin{aligned}\frac{d}{dt}\begin{bmatrix}\bar{\mathbf{a}}(t)\\ \bar{\mathbf{b}}(t)\end{bmatrix} = &-\left(\begin{bmatrix}\mathbf{c} & 0\\ 0 & -\mathbf{c}\end{bmatrix}\otimes\mathbf{P}^{-1}\mathbf{Q}\right)\begin{bmatrix}\bar{\mathbf{a}}(t)\\ \bar{\mathbf{b}}(t)\end{bmatrix}\\ &-(\mathbf{K}_1\otimes\mathbf{I}_{N+1})\begin{bmatrix}\bar{\mathbf{a}}(t)\\ \bar{\mathbf{b}}(t)\end{bmatrix}\\ &-(\mathbf{K}_2\otimes\mathbf{I}_{N+1})\frac{1}{\sqrt{\pi t}} * \frac{d}{dt}\begin{bmatrix}\bar{\mathbf{a}}(t)\\ \bar{\mathbf{b}}(t)\end{bmatrix}\end{aligned} \tag{12}$$

where $\bar{\mathbf{a}}(t), \bar{\mathbf{b}}(t)$ collect all the nodal values of the wave vectors along the line, $\mathbf{I}_\kappa$ is the identity matrix of order κ, and $\otimes$ indicates the Kronecker matrix product [30]. The definition of the latter is briefly recalled in Appendix A.

We turn now to the insertion of the termination equations into the scheme. The guidelines for the boundary treatment are generality, simplicity, stability, and preservation of high order accuracy also at the edges of the line. The first two requirements indicate that any type of termination should be allowed, but the practical implementation should be as simple and possible. The last two requirements are related to two important features that may be difficult to enforce at the same time. Indeed, both theoretical and numerical evidence has been given that a conventional boundary treatment (based on the elimination of some border variables using the termination equations) allows a global high-order approximation but may result unstable [28]. For this reason, we concentrate on an alternative procedure for the terminations based on a weak treatment. We detail this procedure below.

We refer to Fig. 2 for the definition of the border variables involved in the boundary implementation. We indicate with $\mathbf{a}_0(t)$, $\mathbf{b}_0(t), \mathbf{a}_N(t)$, and $\mathbf{b}_N(t)$ the nodal values of the scattering waves at the edges of the MTL segment. The incident waves into the left and right terminations are, respectively, $\mathbf{b}_{0,\mathrm{inc}}(t)$ and $\mathbf{a}_{N,\mathrm{inc}}(t)$, while the reflected waves from the left and right terminations are, respectively, $\mathbf{a}_{0,\mathrm{ref}}(t)$, $\mathbf{b}_{N,\mathrm{ref}}(t)$. In order to comply with the above described requirements, we directly excite the terminations with the nodal values of the waves exiting the MTL, i.e., we set

$$\begin{cases}\mathbf{b}_{0,\mathrm{inc}}(t) = \mathbf{b}_0(t)\\ \mathbf{a}_{N,\mathrm{inc}}(t) = \mathbf{a}_N(t).\end{cases}$$

The reflected waves are computed through the state equations of the termination networks

$$\begin{cases}\mathbf{H}_0\frac{d}{dt}\mathbf{x}_0(t) = \mathcal{F}_0(\mathbf{x}_0(t), \mathbf{b}_0(t), \mathbf{u}_0(t)),\\ \mathbf{a}_{0,\mathrm{ref}}(t) = \mathcal{G}_0(\mathbf{x}_0(t), \mathbf{b}_0(t), \mathbf{u}_0(t)),\end{cases}$$
$$\begin{cases}\mathbf{H}_N\frac{d}{dt}\mathbf{x}_N(t) = \mathcal{F}_N(\mathbf{x}_N(t), \mathbf{a}_N(t), \mathbf{u}_N(t)),\\ \mathbf{b}_{N,\mathrm{ref}}(t) = \mathcal{G}_N(\mathbf{x}_N(t), \mathbf{a}_N(t), \mathbf{u}_N(t)).\end{cases} \tag{13}$$

We define, then, the left and right termination errors as

$$\begin{cases}\mathbf{\Xi}_0(t) = \mathbf{a}_0(t) - \mathbf{a}_{0,\mathrm{ref}}(t)\\ \mathbf{\Xi}_N(t) = \mathbf{b}_N(t) - \mathbf{b}_{N,\mathrm{ref}}(t)\end{cases}$$

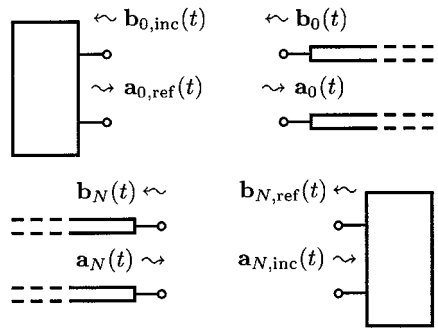

Fig. 2. Border waves involved in the weak boundary treatment.

A conventional boundary treatment would enforce $\mathbf{\Xi}_0(t)$ and $\mathbf{\Xi}_N(t)$ to be vanishing, thus allowing to eliminate the nodal variables $\mathbf{a}_0(t)$ and $\mathbf{b}_N(t)$ from the system. Conversely, the proposed technique does not enforce any constraint on the boundary errors. All the nodal variables are retained in the set of unknowns. The boundary errors $\mathbf{\Xi}_0(t)$ and $\mathbf{\Xi}_N(t)$ are simply weighted by a suitable penalty parameter ω and added to the MTL equations as

$$\begin{aligned}\frac{d}{dt}\begin{bmatrix}\bar{\mathbf{a}}(t)\\ \bar{\mathbf{b}}(t)\end{bmatrix} = &-\left(\begin{bmatrix}\mathbf{c} & 0\\ 0 & -\mathbf{c}\end{bmatrix}\otimes\mathbf{P}^{-1}\mathbf{Q}\right)\begin{bmatrix}\bar{\mathbf{a}}(t)\\ \bar{\mathbf{b}}(t)\end{bmatrix}\\ &-(\mathbf{K}_1\otimes\mathbf{I}_{N+1})\begin{bmatrix}\bar{\mathbf{a}}(t)\\ \bar{\mathbf{b}}(t)\end{bmatrix}\\ &-(\mathbf{K}_2\otimes\mathbf{I}_{N+1})\frac{1}{\sqrt{\pi t}} * \frac{d}{dt}\begin{bmatrix}\bar{\mathbf{a}}(t)\\ \bar{\mathbf{b}}(t)\end{bmatrix}\\ &-\omega\begin{bmatrix}-q_0\,\mathbf{c}\,\mathbf{\Xi}_0(t)\otimes\mathbf{p}_0\\ q_N\mathbf{c}\mathbf{\Xi}_N(t)\otimes\mathbf{p}_N\end{bmatrix}\end{aligned} \tag{14}$$

where $\mathbf{p}_0$ and $\mathbf{p}_N$ are the first and last columns of $\mathbf{P}^{-1}$, respectively. The above expressions, together with the state equations of the terminations, constitute a system of ordinary differential equations (ODEs) where the only variable yet to be discretized is time. It can be rigorously proved (see [2], [27] for a detailed analysis in the static and linear terminations case) that this discretization results in a strictly stable and consistent scheme (of order τ). Therefore, convergence under grid refinement is insured since both the local truncation error and its late time behavior are under control. These convergence properties allow to conclude that also the boundary errors $\mathbf{\Xi}_{0,N}(t)$ remain bounded and tend to zero with order τ. The general stability proof is omitted here for the sake of conciseness but is detailed in Appendix B. As a byproduct of the proof, a guideline for the selection of the penalty parameter ω can be easily determined. For the difference operators that will be used in this paper [3] we have $q_0 = -1/2$ and $q_N = 1/2$. This results in an optimal choice for this parameter $\omega_{\mathrm{opt}} = 2$ regardless of the nature of the termination.

The last step in the discretization process is the selection of a suitable time-stepping algorithm to solve the global system of ODEs. The choice of this scheme must be determined by the eigenspectrum of the system (14), in order to achieve late-time stability [16]. As an example, we report in Fig. 3 the eigenspectrum of an open-circuited line at both ends discretized with a fourth-order SBP explicit difference scheme [3]. It is clear that

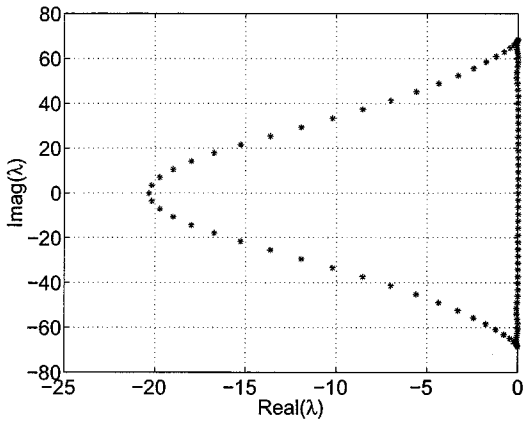

Fig. 3. Eigenspectrum of an open-circuited line discretized $(N = 50)$ with a fourth-order explicit difference scheme.

the standard leapfrog scheme based on centered second-order finite differences in time is not suitable for this spatial discretization. In fact, its stability region (a symmetric interval of the imaginary axis [17], [29]) would not encompass all the eigenvalues due to the spatial discretization and depicted in the plot for the mentioned case. The time discretization scheme to be used for the present application must have a stability region which extends also in the left half complex plane. It turns out that the classical fourth-order Runge-Kutta (RK4) scheme [24] is nearly optimal for our purpose. Its stability region is well-suited to the location of the spatial eigenvalues [16]. Moreover, it is an explicit scheme allowing for recursive time-stepping just like FDTD. Finally, since we are mainly interested in high-order spatial approximation, we also have a high-order (fourth-order) scheme in time. This is obviously a good choice for the discretization of hyperbolic equations like MTLs, where the global accuracy is dictated by the lowest order between space and time discretization. We remark that the Courant condition for the combination of an explicit fourth-order scheme in space with RK4 time-stepping is $\Delta t \leq 2.06\Delta z/c_{\max}$, i.e., almost twice as much as for the standard FDTD scheme [16].

The practical implementation of the RK4 time-stepping scheme that we use in this report takes into account the time-domain convolution terms due to skin-effect losses in an approximate way. A direct application to the integro-differential equation would result indeed too involved and computationally expensive. We detail below the proposed time discretization.

Let us rewrite system (14) as

$$\frac{d}{dt}\bar{\mathbf{y}}(t) = \mathbf{M}(\bar{\mathbf{y}}(t), t) - (\mathbf{K}_2 \otimes \mathbf{I}_{N+1})\frac{1}{\sqrt{\pi}}\mathbf{\Theta}(\bar{\mathbf{y}}, t)$$

where the array $\bar{\mathbf{y}}(t)$ collects all the unknowns, and the vector function $\mathbf{M}$ collects all the terms excluding those related to the high-frequency losses. The latter are reported through the operator $\mathbf{\Theta}$, defined as

$$\mathbf{\Theta}(\bar{\mathbf{y}}, t) = \int_0^t \frac{1}{\sqrt{t-\sigma}}\frac{d}{d\sigma}\bar{\mathbf{y}}(\sigma)\, d\sigma.$$

It should be noted that, if we remove the convolution terms, we get a system of ODEs representing a high-order approximation of the MTL equations with only dc losses

$$\frac{d}{dt}\bar{\mathbf{y}}_{\mathrm{DC}}(t) = \mathbf{M}(\bar{\mathbf{y}}_{\mathrm{DC}}(t), t).$$

Direct application of the RK4 scheme to this system gives the following recursion equation

$$\bar{\mathbf{y}}_{\mathrm{DC}}^{n+1} = \bar{\mathbf{y}}_{\mathrm{DC}}^{n} + \mathbf{\Phi}$$

where the term $\mathbf{\Phi}$ (see, e.g., [24]) represents the correction to be applied to the solution at time step $t_n = n\Delta t$ in order to get the solution at time step $t_{n+1} = (n+1)\Delta t$. This correction is determined through a four-step approximation of the first derivative of the solution throughout the interval $[t_n, t_{n+1}]$, thus leading to fourth-order accuracy. This suggests the form of the approximate time-stepping equation for the solution with the skin effect terms. A centered approximation of the convolution integral is applied as an additional correction term, leading to the update equation

$$\bar{\mathbf{y}}^{n+1} = \bar{\mathbf{y}}^{n} + \mathbf{\Phi} - (\mathbf{K}_2 \otimes \mathbf{I}_{N+1})\frac{1}{\sqrt{\pi}}\mathbf{\Theta}^{n+1/2}$$

where

$$\mathbf{\Theta}^{n+1/2} = \int_0^{t_{n+1/2}} \frac{1}{\sqrt{t_{n+1/2}-\sigma}}\frac{d}{d\sigma}\bar{\mathbf{y}}(\sigma)\, d\sigma.$$

The actual computation of $\mathbf{\Theta}^{n+1/2}$ is performed here through the well-known Prony approximation [21]. The latter is based on a fit of the convolution kernel with exponential functions giving rise to recursive convolution terms. We omit here the standard derivation (see, e.g., [22], [25] for the FDTD case), leading to the final expression

$$\begin{aligned}\bar{\mathbf{y}}^{n+1} = \bar{\mathbf{y}}^{n+1} &+ \left[\left(\mathbf{I}_{2M} + \mathbf{K}_2\sqrt{\frac{2\Delta t}{\pi}}\right)^{-1} \otimes \mathbf{I}_{N+1}\right]\mathbf{\Phi} \\ &- \left[\left(\mathbf{I}_{2M} + \mathbf{K}_2\sqrt{\frac{2\Delta t}{\pi}}\right)^{-1}\mathbf{K}_2\sqrt{\frac{\Delta t}{\pi}} \otimes \mathbf{I}_{N+1}\right]\sum_{i=1}^{m}\mathbf{\Psi}_i^n\end{aligned}$$

where the m auxiliary arrays $\mathbf{\Psi}_i^n$ are computed through the following recursion rule

$$\mathbf{\Psi}_i^n = e^{b_i}\mathbf{\Psi}_i^{n-1} + a_i e^{b_i}(\bar{\mathbf{y}}^n - \bar{\mathbf{y}}^{n-1}). \tag{15}$$

The coefficients $\{(a_i, b_i), i = 1, \ldots, m\}$ represent the m-term Prony approximation of

$$Z_0^*(k) = \int_{k-1/2}^{k+1/2} \frac{d\sigma}{\sqrt{\sigma}}, \quad k \geq 1$$

according to

$$Z_0^*(k) \simeq \sum_{i=1}^{m} a_i e^{b_i k}. \tag{16}$$

We have found that setting $m = 10$ allows to cover with negligible error at least three decades for the parameter k. The corresponding values of a_i and b_i are listed in Table I.

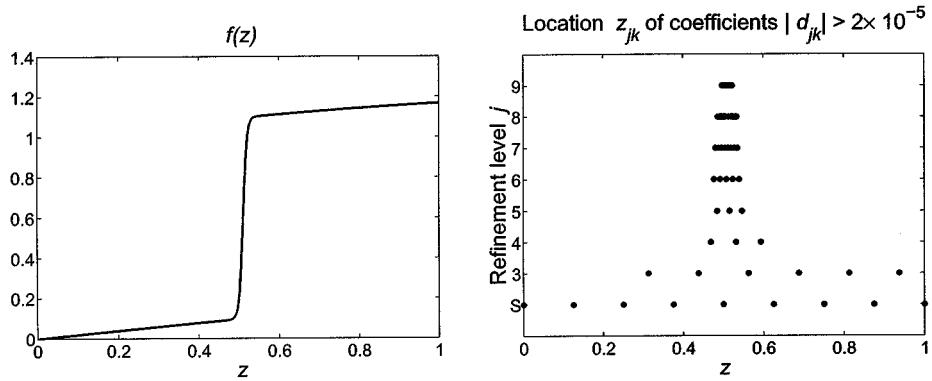

(a) (b)

Fig. 4. Typical transient waveform along: (a) an MTL segment and (b) location of wavelet coefficients larger than $\varepsilon = 2 \times 10^{-5}$.

IV. Adaptive Discretization

This section is devoted to the description of the wavelet expansion that will lead to a sparse representation of the power waves along the MTL. We will show that the structure of transient waveforms typically found on PCBs can be captured with very few significant unknowns, provided that these represent expansion coefficients into some wavelet basis. Working then in a wavelet basis will allow a drastic reduction in the number of operations required to compute the solution for a given fixed accuracy.

Many excellent books and papers exist on wavelets, therefore we will not give a detailed derivation here. For the interested reader, we point to [4]–[6] for general wavelet theory and [7], [8]. and [15] for some details on the sparse approximations that will be used in this paper. In the following paragraphs, we detail the main results that are essential for the presentation of the main algorithm. We detail in separate subsections, the standard definition of a static adaptive approximation through wavelets (Section IV-A) and its application for the definition of a dynamic mesh refinement/coarsening allowing for a sparse computation of the MTL transient solution (Section IV-B).

A. Static Adaptivity

We recall that any finite energy function $f(z)$ can be expanded into a summation of scaling functions $\varphi_{j,k}(z)$ and wavelets $\psi_{j,k}(z)$ according to

$$f(z) = \sum_k s_{j_0,k}\varphi_{j_0,k}(z) + \sum_{j=j_0}^{\infty}\sum_k d_{j,k}\psi_{j,k}(z) \qquad (17)$$

where the index j defines the *refinement level* and the index k selects a specific basis function at a given level. Higher levels describe finer and finer details in the function $f(z)$, while the scaling functions terms at the minimum refinement level j_0 describe a smooth "low frequency" approximation of $f(z)$. Since the summation over levels extends up to ∞, the expansion is exact in the energy norm.

Since we are expanding a function defined on a bounded domain (any practical MTL has finite length) we cannot express the single scaling functions and wavelets through the usual dilations and translations of a single mother scaling function and wavelet. We must resort to a construction of wavelets specifically built on bounded domains. This construction is quite delicate since the many good properties of wavelets may be lost in the definition of those basis functions that are collocated near the edges of the domain. We use in this paper, the wavelet system constructed in [12], specifically biorthogonal B-spline wavelets with two vanishing moments. This system has been explicitly built with special attention to the spatial localization close to the edges. As a result, each wavelet function $\psi_{j,k}(z)$ has a small compact (finite-size) support proportional to 2^{-j} and centered around the location $z_{j,k} = (k + 0.5)2^{-j}$.

In practical applications the summation in (17) cannot extend up to ∞, so a maximum refinement level $J_{\max}$ must be determined *a priori*. In addition, the theory of wavelet-based nonlinear approximations [5], [8] indicates that we can neglect all those wavelet contributions having a small coefficient $d_{j,k}$. Fixing a threshold ε controlling the accuracy of the approximation, we can define a (static) adaptive approximation as

$$f(z) \simeq \sum_k s_{j_0,k}\varphi_{j_0,k}(z) + \sum_{(j,k)\in\Lambda_\varepsilon} d_{j,k}\psi_{j,k}(z) \qquad (18)$$

where the index set Λ_ε is defined as

$$\Lambda_\varepsilon = \{(j,k) : |d_{j,k}| \geq \varepsilon\}$$

and selects those coefficients to be retained in the summation (the "active" coefficients) through hard thresholding. The example reported in Fig. 4 illustrates this adaptive approximation applied to a transient waveform typically found on MTLs carrying fast digital signals (left panel). The right panel indicates with a dot the location $z_{j,k}$ of all the scaling functions and active wavelet coefficients included in the summation, i.e., larger than the threshold $\varepsilon = 2 \times 10^{-5}$. We can note that these significant coefficients extend throughout the domain for low levels, thus recovering the smooth part of the signal. Conversely, as the level j increases, only those coefficients located around the front result larger than the threshold. The others can be neglected without significantly affecting the accuracy of the representation. In fact, for this example the relative norm of the residual results less than 10^{-4}, while only 5% of the total coefficients is used in the expansion.

B. Dynamic Adaptivity

We turn now to the application of the above described adaptive representation to the MTL equations. We impose an additional constraint that the number of spatial nodes $N+1$ in the finite difference discretization of the foregoing section coincides with the total number of coefficients in the wavelet expansion. Choosing a maximum refinement level $J_{\max}$, this corresponds for the specific wavelet system used in this paper to setting $N = 2^{J_{\max}}$. We define then a wavelet transformation matrix $\mathbf{W}$ mapping the nodal values of any given function into the set of the scaling functions and wavelet coefficients up to level $J_{\max}$. Performing this change of basis to each separate power wave in (14) leads to the following expression

$$\begin{aligned}\frac{d}{dt}\begin{bmatrix}\hat{\mathbf{a}}(t)\\ \hat{\mathbf{b}}(t)\end{bmatrix} = &-\left(\begin{bmatrix}\mathbf{c} & 0\\ 0 & -\mathbf{c}\end{bmatrix}\otimes \mathbf{W}\mathbf{P}^{-1}\mathbf{Q}\mathbf{W}^{-1}\right)\begin{bmatrix}\hat{\mathbf{a}}(t)\\ \hat{\mathbf{b}}(t)\end{bmatrix}\\ &-(\mathbf{K}_1\otimes \mathbf{I}_{N+1})\begin{bmatrix}\hat{\mathbf{a}}(t)\\ \hat{\mathbf{b}}(t)\end{bmatrix}\\ &-(\mathbf{K}_2\otimes \mathbf{I}_{N+1})\frac{1}{\sqrt{\pi t}} * \frac{d}{dt}\begin{bmatrix}\hat{\mathbf{a}}(t)\\ \hat{\mathbf{b}}(t)\end{bmatrix}\\ &-\omega\begin{bmatrix}q_0\mathbf{c}\boldsymbol{\Xi}_0(t)\otimes \mathbf{p}'_0\\ -q_N\mathbf{c}\boldsymbol{\Xi}_N(t)\otimes \mathbf{p}'_N\end{bmatrix}\end{aligned} \tag{19}$$

where $\mathbf{p}'_{0,N} = \mathbf{W}\mathbf{p}_{0,N}$. The vectors $\hat{\mathbf{a}}(t)$ and $\hat{\mathbf{b}}(t)$ collect all the scaling functions and wavelets coefficients of the solution. This system is fully equivalent to (14), but the solution is expressed in a wavelet basis.

As a consequence of the wavelet representation, the vectors of unknowns $\hat{\mathbf{a}}(t)$ and $\hat{\mathbf{b}}(t)$ can be very sparse at any fixed time t. Therefore, only a small subset of system (19) is actually needed for the computation of the solution in the overall time-stepping scheme, since many operations reduce to multiplication by zeros. A smart use of sparse matrices allows then to compute the solution with a much reduced number of operations. Some important issues related to this sparse time-stepping strategy are discussed in the following paragraphs.

We use forward and backward propagating modal waves for the description of the electrical status of the line. The propagation of each mode is almost independent from any other mode, with the only coupling being provided by losses (see the diagonalization procedure in Section II). This coupling is quite weak for realistic structures, even in the case of moderately high losses. Therefore, we can assume that each separate mode should be characterized by its own set of active wavelet coefficients. At each time step we then perform a hard thresholding of wavelet coefficients for each separate mode, therefore obtaining a total of $2M$ separate sets of indices. This is the minimal set of coefficients strictly needed for an accurate representation of the solution.

There are some coefficients that must be kept active at all time iterations regardless of the structure of the solution. These can be collected in two different classes itemized below.

1) The scaling function coefficients at the minimum refinement level j_0. These coefficients allow to recover the low-frequency behavior of the solution, and correspond to a coarse discretization mesh. Due to the construction of wavelet systems on bounded domains these coefficients are always required. However, their number may be very small according to the particular type of wavelets employed in the simulation. In this paper we, set $j_0 = 4$, thus obtaining 17 scaling function coefficients per mode.
2) The first wavelet coefficient near each boundary at any refinement level up to the maximum level $J_{\max} - 1$. These coefficients are necessary since they allow to capture the possibly fast variations induced by the lumped sources or by the non linearities at the terminations of the line. Since the waveforms launched into the line are not known a priori, the adaptive algorithm must be conservative and compute in any case at least one coefficient (one is sufficient) at all refinement levels. The number of these coefficients is $J_{\max} - j_0$ per termination.

The particular choice of the threshold ε which is best suited for the simulation depends on the features of the sources exciting the line (rise time) and on the strength of the non linearities present in the terminations. An additional degree of freedom in the thresholding procedure could be provided by a level-dependent threshold $\varepsilon(j)$. This would allow a fine-tunable selectivity over different spatial (and therefore temporal) scales. We have performed several tests with different types of scale-dependent thresholds, without noting significant advantages with respect to the simpler uniform threshold. Therefore, all the numerical examples that will be presented in the forthcoming section are obtained with a fixed threshold.

Once the set of active coefficients at time $t_n = n\Delta t$ (we will denote it as Λ_ε^n) has been determined, it is possible to guess a priori which will be the set of active coefficients at the next iteration t_{n+1}. More precisely, it is possible to determine an enlarged set $\tilde{\Lambda}_\varepsilon^{n+1}$ that strictly includes the actual set of indices $\Lambda_\varepsilon^{n+1}$ that is expected to be significant at the next time iteration. This is a consequence of the finite propagation speed intrinsic in the MTL equations, which allows any singularity to move forward or backward of a finite extent. More precisely, let us assume that a singularity is located around $z = \xi_n$ at time t_n. Assuming a maximum modal propagation speed equal to $c_{\max}$, we see that the singularity will be located at time t_{n+1} at a point $z = \xi_{n+1}$ within the interval $[\xi_n - c_{\max}\Delta t, \xi_n + c_{\max}\Delta t]$. In particular, if the time-stepping is performed at a Courant number $p \le 1$, which is the case for all the numerical examples presented in this paper, we conclude that the interval extends in both directions less than the finest resolution $\Delta z = 2^{-J_{\max}}$ employed in the discretization. The conclusion translates into a simple rule for the determination of the set $\tilde{\Lambda}_\varepsilon^{n+1}$: if a coefficient $d_{j,k}$ is active at time t_n, include in the set of coefficients to be computed at the next time iteration the three coefficients $d_{j,k-1}$, $d_{j,k}$, and $d_{j,k+1}$. A more precise and abstract definition of set $\tilde{\Lambda}_\varepsilon^{n+1}$ can be given as

$$\tilde{\Lambda}_\varepsilon^{n+1} = \mathcal{E}\left\{\Lambda_\varepsilon^n\right\}$$

where the extension operator $\mathcal{E}$ is defined as

$$(j,k) \in \Lambda_\varepsilon^n \Rightarrow \{(j,k-1),(j,k),(j,k+1)\} \in \tilde{\Lambda}_\varepsilon^{n+1}.$$

It should be noted that the addition of one coefficient on the left and on the right allows to capture the inevitable distortion

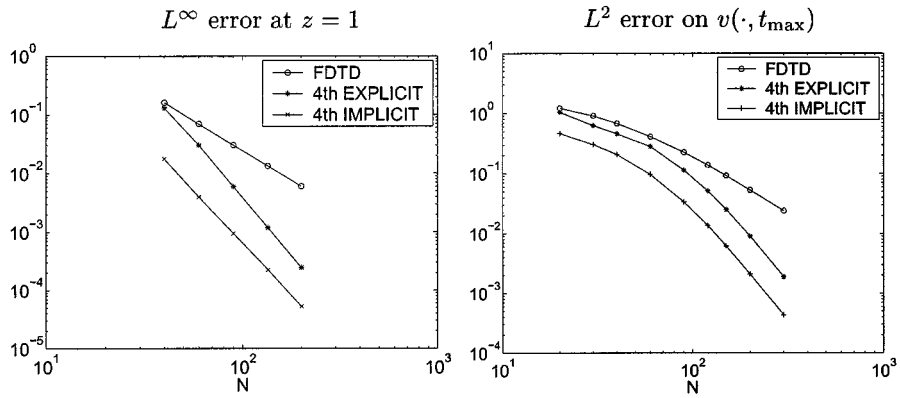

(a) (b)

Fig. 5. Comparison between FDTD and fourth-order schemes with RK4 time stepping applied to a unmatched scalar transmission line. (a) The L^∞ error on the termination voltage at the right boundary (Gaussian source). (b) The L^2 error of the voltage distribution along the line at the final time $t_{\max} = 10$ (step source).

in the waveform of each mode due to the effects of frequency-dependent losses.

In case of high losses, there may be quite significant distortions of the modal waveforms during their propagation due to the nonlocal effects of the convolution kernel related to the internal impedance. Consequently, a more refined definition of the set $\tilde{\Lambda}_\varepsilon^{n+1}$ may be obtained through iterative application of the extension operator

$$\tilde{\Lambda}_\varepsilon^{n+1} = \mathcal{E}_r \left\{\Lambda_\varepsilon^n\right\}$$

where

$$\mathcal{E}_r\{\,\cdot\,\} = (\mathcal{E} \circ \mathcal{E} \circ \cdots \circ \mathcal{E})\{\,\cdot\,\} = \mathcal{E}\{\mathcal{E}\{\cdots \mathcal{E}\{\,\cdot\,\}\}\}.$$

The value $r = 1$ is sufficient in case of distortionless propagation. Conversely, larger values may be used for getting a more precise but less sparse representation of the solution. The several tests that we performed lead to the conclusion that setting $r = 1$ or $r = 2$ works well in most cases of practical interest, even with high losses.

An additional remark about the location of active coefficients is in order. Strong theoretical arguments on the structure of Sobolev and Besov function spaces [5], [7], [8] indicate that the decay of the wavelet coefficients for increasing level j depends on the local regularity of the function being approximated. As we pointed in Section IV–A, local smoothness implies fast decay, while local singularities (to be intended in broad sense as regions of faster variations in f or its derivatives) imply slower decay. When looking then at fast digital signals, where the "singularities" correspond to the rising or falling edges due to logic transitions, it turns out that the index set Λ_ε is practically tree-structured. If a coefficient $d_{j,k}$ is active, then also its "father" coefficient $d_{j-1,\lceil k/2 \rceil}$ must be active, where $\lceil \alpha \rceil$ indicates the smallest integer larger than α. This fact can be used on one hand to produce efficient indexing algorithms and memory handling. In addition, the proposed extension operator $\mathcal{E}$ (and consequently its refined version $\mathcal{E}_r$) preserves this property: if Λ_ε^n is tree-structured, then also $\tilde{\Lambda}_\varepsilon^{n+1}$ is tree-structured.

Insofar we have detailed the sparse representation of the solution and the algorithm allowing for the sparse update of the wavelet coefficients, thus avoiding the computation of those coefficients that will be negligible at the next time iteration. However, we should point that also the auxiliary vectors $\mathbf{\Psi}_n^i$ of (15) used for the Prony approximation of the skin-effect terms should be approximated with a sparse representation. Otherwise, the effectiveness of the adaptive algorithm would be wasted in case of ac losses. It turns out that the recurrence rule (15) relates each of these vectors to the time derivative of the unknowns. The time derivatives are large exactly where the fast variations of the solution occur. Therefore, we can use also for the auxiliary vectors $\mathbf{\Psi}_n^i$ the index sets already in use for the representation of the solution. This is a considerable advantage since it simplifies the adaptive indexing algorithm.

We summarize below the key steps to be performed at each iteration.

1) At iteration n start with a set of active indices Λ_ε^n.
2) Predetermine the set $\tilde{\Lambda}_\varepsilon^{n+1}$ through application of the extension operator $\mathcal{E}_r$. Note that this step consists only on indexing and/or memory handling, therefore only few operations involving integers or pointers are necessary, with a negligible computational overhead.
3) Apply the time-stepping procedure detailed in Section III to compute $\bar{\mathbf{y}}^{n+1}$. Use for computations only the coefficients in $\bar{\mathbf{y}}^n$ indexed by Λ_ε^n. Compute only the coefficients indexed by $\tilde{\Lambda}_\varepsilon^{n+1}$. The others will be negligible and do not need to be computed.
4) Perform a hard thresholding on the set of coefficients that have just been computed at previous step, i.e., determine a new set of indices $\Lambda_\varepsilon^{n+1} \subseteq \tilde{\Lambda}_\varepsilon^{n+1}$ such that all its coefficients are larger than ε. This step allows coarsening of the adaptive mesh once a singularity has moved away.
5) Start again from Step 1 until the end of the simulation has been reached.

Additional considerations on the proposed algorithm will be found as comments for the numerical tests to be presented in Section V.

V. Numerical Results

We begin illustrating the behavior of two fourth-order finite-difference nonadaptive schemes with a test case. This example is intended to show the accuracy improvement that can be achieved with high order differences with respect to standard FDTD modeling. A normalized lossless scalar transmission line (with char-

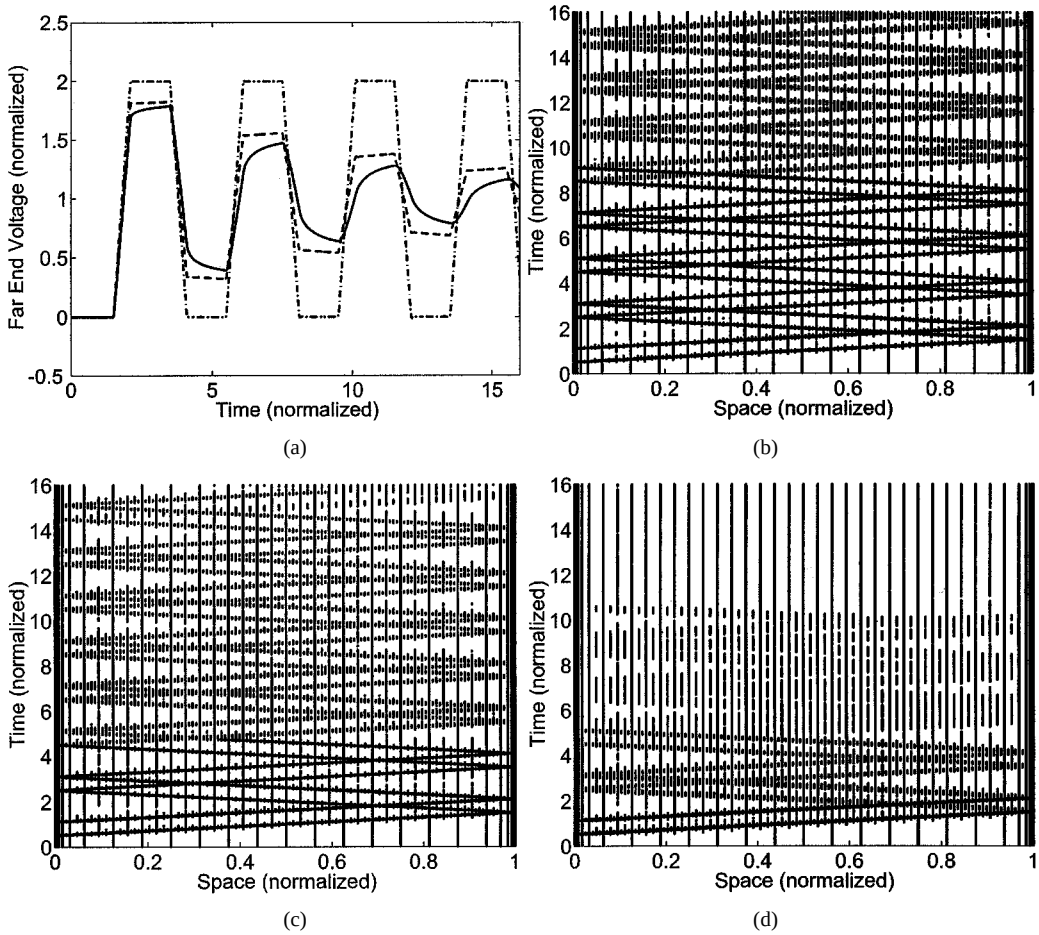

Fig. 6. Wavelet-adaptive simulation of a normalized scalar transmission line excited by an ideal step voltage source with finite rise time. (a) Far-end voltages obtained in the lossless case (dash-dotted line), with dc losses (dashed line), and skin-effect losses (continuous line). Corresponding locations $z_{j,k}$ of active wavelet coefficients (b) lossless, (c) dc losses, and (d) skin effect losses. For convenience, the locations $z_{j,k}$ for both forward and backward propagating modes are superimposed on the same plot.

acteristic impedance $Z_c = 1$, propagation delay time $T_D = 1$, and propagation speed $c = 1$) is terminated by two highly unmatched resistances $R_S = 10^{-3}, R_L = 10^3$, i.e., $\Gamma_S = -0.998$, $\Gamma_L = 0.998$. The left panel of Fig. 5 reports the maximum error at the right boundary between the exact solution and the numerical solution obtained with FDTD and with two (explicit and implicit) fourth-order schemes with RK4 time advancement, using a gaussian (semi-width $\sigma_s = 0.08$) pulse voltage source. The Courant number was set in all cases to $p = 0.8$, i.e., close to the stability limit of the FDTD scheme. It is evident that the fourth order schemes perform much better than FDTD in terms of both error values and decay rate under grid refinement. It can be seen from the plot that the achievement of a maximum error below a given threshold, say $\delta = 10^{-3}$, would require a very fine grid or, equivalently, a very large number of unknowns for the FDTD method (as the decay rate is N^{-2}, a simple extrapolation gives approximately $N = 700$). The same error can be obtained with the fourth-order schemes with much less grid points, about $N = 140$ for the explicit one and $N = 90$ for the implicit one. The right panel reports the L^2 error on the voltage distribution along the line at the final simulation time using a step source with rise time $\tau_r = 0.1T_D$. For small values of N (insufficient resolution for all three schemes) the numerical dispersion strongly affects the solution. When the discretization becomes adequate the error curves exploit a slope change, approaching the asymptotic behavior for both FDTD (-2) and the two fourth-order schemes (-4).

We illustrate now through another test problem the capabilities of the wavelet-based adaptive algorithm presented in this paper. A normalized scalar transmission line as above is excited through an ideal step voltage source (zero internal resistance) with rise time $\tau_r = 0.6T_D$. The line is open-circuited at the far end. Three simulations were performed, in order to illustrate the behavior of the proposed scheme in case of lossy structures. The first case is lossless, i.e., we set $A = B = 0$ in the expressions for the internal impedance. The second case includes only dc losses. We deliberately chose a moderately high loss structure, setting $A = 0.2$. The last case includes both dc and ac losses through addition of the skin effect terms in the internal impedance with $B = 0.1$. The results are depicted in Fig. 6. The top left panel reports the far end voltage for the three simulations. We remark that validations with the standard FDTD scheme have been performed for all numerical examples presented in this paper. In the present case, as well as for all other tests we performed, there was no visible difference in the simulation results. Therefore, we do not report in the plots the FDTD curves since they would be undistinguishable from the outcome of the presented scheme. The other three panels of Fig. 6 show the locations $z_{j,k}$ of active coefficients automatically determined by the adaptive algorithm and used for

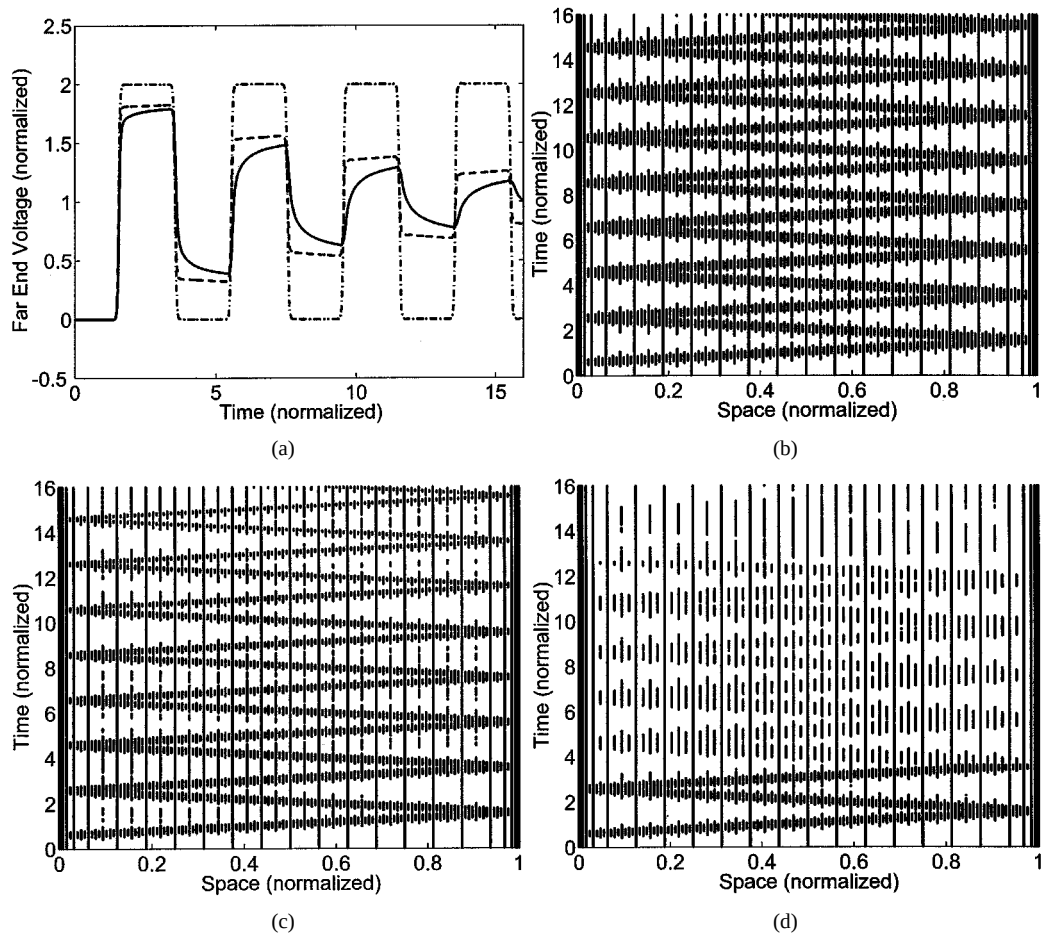

Fig. 7. As in Fig. 6, but with a smoothed step voltage source expressed by (20).

the computation of the solution. The threshold that was used in this case is $\varepsilon = 1 \times 10^{-5}$. Some considerations are in order. First, the active coefficients are placed in all cases along the characteristic curves where the singular points of the propagating waves are located. This is expected since these are exactly the coefficients predicted by wavelet theory to be large and significant for the description of the solution. The other coefficients are smaller than the threshold and were neglected in the simulation. Second, in the lossy cases (bottom panels) the distributed losses cause a weakening of the singularities. The active wavelet coefficients get smaller and smaller as time progresses in the simulation, up to the point where the number of refinement levels needed for the representation of the solution decreases. This effect is particularly evident in the case of ac losses (bottom right panel) due to the smoothing effect induced by the high-frequency behavior of the internal impedance. It should be noted that this reduction in the number of active coefficients does not affect the overall accuracy of the simulation.

A second set of simulations was performed to test the robustness of the algorithm with another type of excitation waveform. The voltage source was set to a smoothed step with expression

$$V_S(t) = \frac{1}{2} V_p \left\{ 1 + \tanh \frac{2(t - T_s - \tau_r/2)}{\tau_r} \right\} \qquad (20)$$

where $V_p = 1$ is the amplitude, $T_s = 0.5$ is the onset time and $\tau_r = 0.05$ is the rise time. This smoother waveform is a more realistic modeling tool for electrical interconnects typically found on PCBs. The results for the normalized scalar line with no losses, dc losses, and ac losses are reported in Fig. 7. The same considerations and comments that apply to previous case can be repeated for the present example as well.

The next example illustrates the behavior of the scheme for a multiconductor structure. Again, the structure is normalized with a unitary length. The per-unit-length matrices

$$\mathbf{L} = \begin{bmatrix} 1 & 0.5 \\ 0.5 & 1 \end{bmatrix}, \quad \mathbf{C} = \begin{bmatrix} 1 & -0.2 \\ -0.2 & 4 \end{bmatrix}$$

determine two different modes with normalized speed equal to $c_1 = 1.17$ and $c_2 = 0.496$, respectively. The corresponding normalized characteristic impedances are $z_1 = 0.803$ and $z_2 = 0.651$. The only losses that are modeled are due to the internal impedance, whose normalized values are

$$\mathbf{A} = \mathbf{B} = \begin{bmatrix} 0.2 & 0.1 \\ 0.1 & 0.2 \end{bmatrix}.$$

One of the two signal conductors of the line is excited by an ideal step voltage source $V_{S1}(t)$ with normalized rise time $\tau_r = 0.6$ at the left termination, with the other conductor shorted to the reference on the same side. The line is left open-circuited at the far end. This configuration results in a boundary equation for the left termination reading

$$\mathbf{a}(0,t) = -\mathbf{b}(0,t) + \begin{bmatrix} 1.064 \\ 0.128 \end{bmatrix} V_S(t)$$

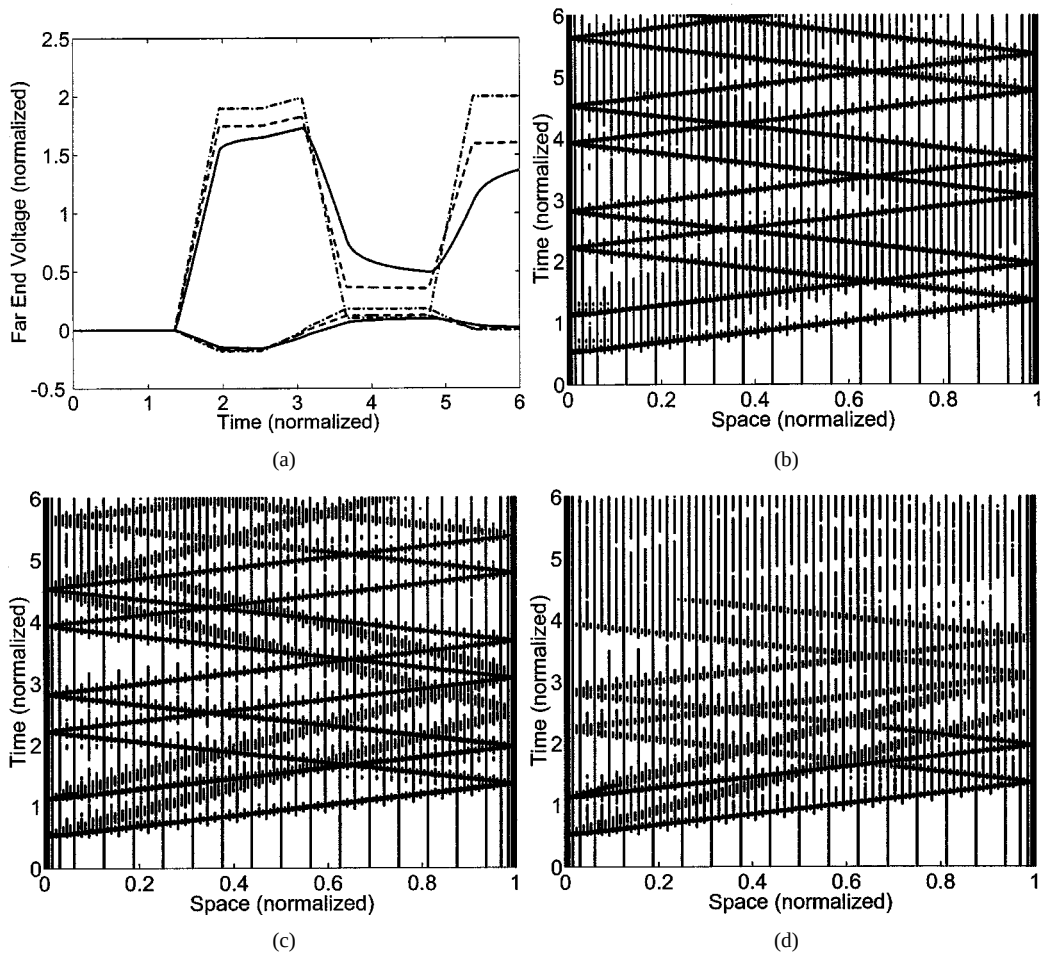

Fig. 8. (a) Far-end voltages for a normalized multiconductor line excited by a step voltage source with finite rise time, obtained in the lossless case (dash-dotted line), with dc losses (dashed line) and with skin effect losses (continuous line). The corresponding locations $z_{j,k}$ of active wavelet coefficients (b) lossless, (c) dc losses, and (d) skin effect losses. For convenience the locations of all forward and backward propagating modes are superimposed on the same plot.

from which we can note that the excitation coefficient for the fast mode is much larger (almost one order of magnitude) than the corresponding coefficient for the slow mode. This is confirmed by the results depicted in Fig. 8. The top left panel reports the far end voltages on both conductors, while the other panels report the locations $z_{j,k}$ of active wavelet coefficients in case of no losses, dc losses and ac losses. The presence of two separate modes with different propagation velocities is evident from the two sets of lines in the space-time plane with different slopes, along which the wavelet coefficients crowd. The active coefficients are more densely distributed along the characteristic curves of the most excited mode, since its singularities are stronger. The other mode moves more slowly and has fewer coefficients. Moreover, as for the scalar line, when losses are included the number of active coefficients decreases with time, since they become eventually not necessary for an accurate representation of the solution.

We turn now to the simulation of structures of practical interest. We first consider a high-loss interconnect made of two PCB lands (width $w = 20$ μm, thickness $t = 10$ μm, separation $s = 20$ μm) over a silicon substrate ($\varepsilon_r = 12$, thickness $\Delta = 100$ μm). The line is 20-cm long and is terminated with 50 Ω loads (this example is taken from [22], p. 329). The excitation is a smoothed step [see(20)] with a very fast rise time

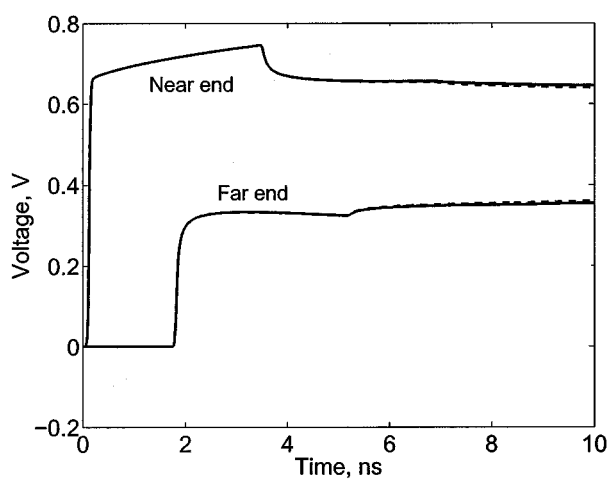

Fig. 9. Termination voltages for a high-loss coplanar line obtained with fourth-order explicit differences (continuous line) and standard FDTD scheme (dashed line).

$\tau_r = 50$ ps. Fig. 9 reports the termination voltages obtained with a fourth-order scheme and with the standard FDTD scheme. Both schemes give practically the same output waveforms. In order to illustrate and quantify the amount of saving in computational effort allowed by the adaptive algorithm, the number

TABLE II
THE NUMBER OF MFLOPS EMPLOYED BY THE WAVELET-ADAPTIVE ALGORITHM IS REPORTED FOR VARIOUS THRESHOLD VALUES ε FOR THE SIMULATION OF AN INTERCONNECT WITH DIFFERENT TYPES OF LOSSES. THE SECOND ROW REPORTS THE MFLOPS EMPLOYED BY THE CORRESPONDING NON-ADAPTIVE ALGORITHM BASED ON NODAL FINITE-DIFFERENCES

Mflops	No losses	DC losses	AC losses
Nodal	42.3	54.8	109
$\varepsilon = 10^{-6}$	20.8	20.3	26.6
$\varepsilon = 2 \times 10^{-6}$	17.5	17.9	23.9
$\varepsilon = 4 \times 10^{-6}$	15.9	15.8	21.3

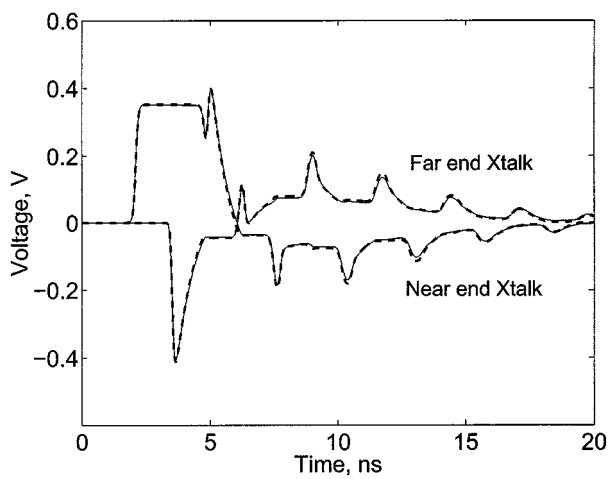

Fig. 10. Crosstalk voltages for a lossy MTL structure terminated with a nonlinear and dynamic load obtained with fourth-order explicit differences (continuous line, including skin-effect losses) and SPICE (dashed line, lossless).

of floating point operations required by the simulations are reported in Table II for different values of the threshold ε and for different types of losses. The table shows a significant reduction of computational effort with respect to the corresponding nodal finite-difference scheme. The wavelet-adaptive scheme is most convenient when skin effect losses are included, since the solution undergoes a regularization and a smoothing, and therefore the number of required coefficients reduces significantly as time progresses.

The last example is a multiconductor lossy interconnect loaded with a nonlinear and dynamic termination network. Three equally spaced PCB lands (width $w = 15$ mil, thickness $t = 1.38$ mil, separation $s = 45$ mil) are placed over a glass epoxy substrate 47-mil thick. One of the side conductors acts as a reference. The middle conductor is excited by 50-Ω step voltage source with rise time $\tau_r = 200$ ps and terminated into an input port of a low-voltage CMOS buffer. The port specifications have been extracted by the IBIS model of the device. The port is modeled by an input capacitance $C_{\rm in} = 5.67$ pF, together with power and ground clamps. We have verified that the parasitic parameters due to the package have a negligible effect on the transient waveforms for this configuration. The other conductor is terminated in 50-Ω resistors. The near-end and far-end crosstalk voltages have been computed through the wavelet-adaptive algorithm based on a fourth-order explicit difference operator. The results are reported in Fig. 10 and compared to a (lossless) SPICE simulation. It can be noted that losses have a negligible effect for this structure. The number of floating point operations required for some combinations of wavelet threshold ε and extension parameter r are reported in Table III. Also in this case the reduction of operations with respect to the nonadaptive simulation based on nodal variables is significant both in the lossless and in the lossy case. The dependence on the extension parameter r is quite weak since skin-effect losses do not induce significant waveform distortions. Conversely, the dependence on ε indicates that larger values of the threshold allow more selectivity in the determination of the active wavelet coefficients, and thus fewer operations. We point out that no visible difference can be noticed between the reference solution (with no adaptivity) and the solution obtained with wavelet thresholding for all cases listed in the table.

TABLE III
THE NUMBER OF MFLOPS EMPLOYED BY THE WAVELET-ADAPTIVE ALGORITHM IS REPORTED FOR VARIOUS THRESHOLD ε AND EXTENSION PARAMETER r VALUES FOR THE SIMULATION OF A LOSSY MTL LOADED WITH A NONLINEAR AND DYNAMIC TERMINATION

Mflops	Lossless	Lossy
Nodal	56	166
$\varepsilon = 2 \times 10^{-5}$, $r = 1$	18.4	38.4
$\varepsilon = 2 \times 10^{-5}$, $r = 2$	19.5	40.0
$\varepsilon = 2 \times 10^{-5}$, $r = 3$	20.7	41.6
$\varepsilon = 5 \times 10^{-5}$, $r = 1$	16.8	35.7
$\varepsilon = 5 \times 10^{-5}$, $r = 2$	16.9	36.6
$\varepsilon = 5 \times 10^{-5}$, $r = 3$	17.3	36.7
$\varepsilon = 1 \times 10^{-4}$, $r = 1$	15.4	34.0
$\varepsilon = 1 \times 10^{-4}$, $r = 2$	15.8	34.8
$\varepsilon = 1 \times 10^{-4}$, $r = 3$	16.0	35.0

VI. CONCLUSION

We have presented a new algorithm for the transient analysis of lossy interconnects typically found on PCB structures. The proposed approach has several advantages with respect to standard modeling tools like, e.g., FDTD. First, both the space and time discretizations are performed through high-order schemes, leading to a high-order convergence rate under grid refinement. Second, the special treatment of the line terminations, which are included in the numerical scheme through a weak approximation, allows to prove rigorously the strict (late time) stability of the scheme. Third, a wavelet expansion of the waves traveling along the interconnect allows a very sparse representation of the solution at each time step. Fourth, the special features of the MTL equations allow a dynamic mesh refinement/coarsening through addition/elimination of wavelet coefficients from the set of unknowns. This adaptivity is performed by means of simple algorithms and allows the computation of the transient solution using a minimal set of strictly necessary coefficients. The presented numerical tests show both a significant accuracy improvement and reduction of computational costs when compared with standard nonadaptive schemes. For this reason, we believe that the presented schemes may be considered as valid alternatives to existing modeling tools in order to reduce the computational burden of interconnects and PCBs characterization.

APPENDIX A
KRONECKER MATRIX PRODUCT

We recall here the definition of the Kronecker matrix product [30], together with a few useful properties that are necessary for the derivations reported in the paper. Given a $p \times q$ matrix A and an arbitrary matrix B, the Kronecker product is defined as

$$A \otimes B = \begin{pmatrix} a_{11}B & \cdots & a_{1q}B \\ \vdots & & \vdots \\ a_{p1}B & \cdots & a_{pq}B \end{pmatrix}.$$

Some related properties are

$$\begin{aligned} &(A \otimes B)(C \otimes D) = (AC) \otimes (BD) \\ &(A \otimes B)^T = A^T \otimes B^T \\ &(A \otimes B)^{-1} = A^{-1} \otimes B^{-1}. \end{aligned} \tag{21}$$

It is easy to show that, if A is a $N \times N$ and B is a $P \times P$ matrix, we have

$$(I_P \otimes A)(B \otimes I_N) = (B \otimes I_N)(I_P \otimes A).$$

Finally, we report a result on the eigenvalues of the Kronecker product

$$Au = \lambda u, \quad Bv = \mu v \Rightarrow (A \otimes B)(u \otimes v) = \lambda\mu(u \otimes v)$$

i.e., each eigenvalue of $A \otimes B$ is the product of an eigenvalue of A and an eigenvalue of B. The corresponding eigenvector is the Kronecker product of the two eigenvectors. This implies that, if both A and B are semipositive definite, also $A \otimes B$ is semipositive definite.

APPENDIX B
STABILITY OF THE BOUNDARY TREATMENT

We prove in this appendix the strict (late time) stability of the proposed discretization and boundary treatment in case of nonlinear and dynamic terminations. We will first investigate the case of a lossless line of length $\mathcal{L}$, therefore we start with (9) and (14) by setting $\mathbf{K}_1 = \mathbf{K}_2 = \mathbf{0}$. Also, without loss of generality, we terminate the line with a linear static termination at the left boundary (with reflection coefficient matrix $\mathbf{\Gamma}_0$) and with a general nonlinear and dynamic termination at the right boundary, expressed by (13). Since we are interested in stability issues, we switch off the internal sources of the terminations, and we consider the time evolution of the global energy stored in the system.

We first define a continuous energy functional related to the exact solution of (9)

$$\begin{aligned} &E_{\text{cont}}(t) \\ &\quad = \int_0^{\mathcal{L}} \{\mathbf{a}^T(z,t)\mathbf{c}^{-1}\mathbf{a}(z,t) + \mathbf{b}^T(z,t)\mathbf{c}^{-1}\mathbf{b}(z,t)\}\, dz \\ &\qquad + \frac{1}{2}\mathbf{x}_N^T(t)\mathbf{H}_N\mathbf{x}_N(t) \end{aligned} \tag{22}$$

where the integral along z reports the energy stored in the line and the last term defines the energy stored in the dynamic elements of the right termination. We then define the dissipation rate of this energy $\mathcal{D}_{\text{cont}}(t) = (d/dt)E_{\text{cont}}(t)$. A straightforward computation involving left multiplication of (9) by the array $[\mathbf{a}^T(z,t)\mathbf{c}^{-1}, \mathbf{b}^T(z,t)\mathbf{c}^{-1}]$ and integration along z leads to

$$\begin{aligned} &\mathcal{D}_{\text{cont}}(t) \\ &\quad = -\mathbf{b}_0^T(t)\left(\mathbf{I}_M - \mathbf{\Gamma}_0^T\mathbf{\Gamma}_0\right)\mathbf{b}_0(t) - \mathbf{a}_N^T(t)\mathbf{a}_N(t) \\ &\qquad + [\mathcal{G}_N(\mathbf{x}_N(t), \mathbf{a}_N(t), \mathbf{0})]^T\mathcal{G}_N(\mathbf{x}_N(t), \mathbf{a}_N(t), \mathbf{0})) \\ &\qquad + \mathbf{x}_N^T(t)\mathcal{F}_N(\mathbf{x}_N(t), \mathbf{a}_N(t), \mathbf{0}) \end{aligned} \tag{23}$$

where also the boundary conditions have been used to eliminate the reflected waves from the terminations. The subscripts $_{0,N}$ indicate the nodal values of the scattering waves at the left and right termination, respectively. As expected, since the line is lossless, only energy dissipation terms due to the termination networks are present.

We now introduce a functional defining the energy behavior of the discrete scheme. Its definition recalls (22), but with the continuous (integral) norm replaced by a suitable discrete norm associated with the (positive definite) matrix $\mathbf{P}$ of the spatial differentiation scheme,

$$\begin{aligned} E_{\text{disc}}(t) = \bar{\mathbf{a}}^T(t)(\mathbf{c}^{-1} \otimes \mathbf{P})\bar{\mathbf{a}}(t) + \bar{\mathbf{b}}^T(t)l(\mathbf{c}^{-1} \otimes \mathbf{P})\bar{\mathbf{b}}(t) \\ + \frac{1}{2}\mathbf{x}_N^T(t)\mathbf{H}_N\mathbf{x}_N(t). \end{aligned} \tag{24}$$

Following the same guidelines as for the continuous energy, starting from (14) and using the algebraic properties of the Kronecker matrix product (21), we can determine the discrete energy dissipation rate

$$\begin{aligned} \mathcal{D}_{\text{disc}}(t) = &-\left\{(\omega - 1)\mathbf{a}_0^T(t)\mathbf{a}_0(t) + \mathbf{b}_0^T(t)\mathbf{b}_0(t)\right. \\ &\left. - \omega\mathbf{a}_0^T(t)\mathbf{\Gamma}_0\mathbf{b}_0(t)\right\} \\ &- \left\{\mathbf{a}_N^T(t)\mathbf{a}_N(t) + (\omega - 1)\mathbf{b}_N^T(t)\mathbf{b}_N(t)\right. \\ &- \omega\mathbf{b}_N^T(t)\mathcal{G}_N(\mathbf{x}_N(t), \mathbf{a}_N(t), \mathbf{0})) \\ &\left. - \mathbf{x}_N^T(t)\mathcal{F}_N(\mathbf{x}_N(t), \mathbf{a}_N(t), \mathbf{0})\right\}. \end{aligned} \tag{25}$$

A first look at this expression allows to conclude that the only value for the penalty parameter ω allowing a non positive dissipation rate in case of marginally stable terminations (either short or open circuit) is $\omega = 2$. This value has been used consistently throughout the simulations presented in the paper. Under this condition, we can easily compute the difference between the discrete and continuous dissipation rate

$$\begin{aligned} \Delta\mathcal{D}(t) &= \mathcal{D}_{\text{disc}}(t) - \mathcal{D}_{\text{cont}}(t) \\ &= -\|\mathbf{a}_0(t) - \mathbf{\Gamma}_0\mathbf{b}_0(t)\|^2 \\ &\quad - \|\mathbf{b}_N(t) - \mathcal{G}_N(\mathbf{x}_N(t), \mathbf{a}_N(t), \mathbf{0}))\|^2 \\ &= -\|\mathbf{\Xi}_0(t)\|^2 - \|\mathbf{\Xi}_N(t)\|^2 \le 0 \end{aligned} \tag{26}$$

which results strictly non positive (the brackets $\|\cdot\|$ indicate the usual vector norm). This means that the energy of the discrete system cannot increase more than the energy of the exact solution. Henceforth, if the termination networks are passive, the proposed discretization preserves strict stability. In addition, we see that a difference in the dissipation rate can only occur when the boundary conditions are not exactly satisfied at time t (recall that the proposed boundary treatment is not exact but approximate with boundary errors $\mathbf{\Xi}_{0,N}$). We conclude that the global dynamics of the discrete system tend to kill through additional numerical dissipation any approximation error occurring at the

boundary nodes. This remarkable property is the key fact allowing the high-order convergence rate of the proposed scheme also at the boundaries.

We omit here the details of the stability proof in the lossy cases. However, it is quite easy to see that the terms related to dc losses lead to additional non positive terms in both (23) and (25), thus improving the stability of the scheme. Similarly, the treatment of skin effect losses through Prony approximation is also stable since the exponents b_i in (16) and Table I are strictly negative.

REFERENCES

[1] M. H. Carpenter, D. Gottlieb, and S. Abarbanel, "The stability of numerical boundary treatments for compact high-order finite-difference schemes," *J. Comput. Phys.*, vol. 108, no. 2, pp. 272–295, 1993.

[2] ——, "Time-stable boundary conditions for finite-difference schemes solving hyperbolic systems: Methodology and application to high-order compact schemes," *J. Comput. Phys.*, vol. 111, no. 2, pp. 220–236, 1994.

[3] M. H. Carpenter, J. Nordström, and D. Gottlieb, "A stable and conservative interface treatment of arbitrary spatial accuracy," *J. Comput. Phys.*, vol. 148, no. 2, pp. 341–365, 1999.

[4] A. Cohen, I. Daubechies, and J. Feauveau, "Biorthogonal bases of compactly supported wavelets," *Comm. Pure Appl. Math.*, vol. 45, no. 5, pp. 485–560, 1992.

[5] W. Dahmen, "Wavelet and multiscale methods for operator equations," *Acta. Numerica.*, vol. 6, pp. 55–228, 1997.

[6] I. Daubechies, *Ten Lectures on Wavelets*. Philadelphia, PA: SIAM, 1992.

[7] R. DeVore, B. Jawerth, and V. Popov, "Compression of wavelet decompositions," *American J. Math.*, vol. 114, no. 4, pp. 737–785, 1992.

[8] R. DeVore, "Nonlinear approximation," *Acta. Numerica.*, vol. 7, pp. 51–150, 1998.

[9] S. Grivet-Talocia and F. Canavero, "Wavelet-based adaptive solution for the nonuniform multiconductor transmission lines," *IEEE Microwave Guided Wave Lett.*, vol. 8, pp. 287–289, Aug. 1998.

[10] ——, "Wavelet-based adaptive simulation of nonuniform interconnects with arbitrary loads," in *Proc. IEEE Int. Symp. EMC 1999*, Seattle, WA, pp. 450–455.

[11] ——, "Accuracy of propagation modeling on transmission lines," in *Proc. IEEE Int. Symp. EMC 1999* , Seattle, WA, pp. 474–479.

[12] S. Grivet-Talocia and A. Tabacco, "Wavelets on the interval with optimal localization," *Math. Model. Methods Appl. Sci.*, vol. 10, pp. 441–462, 2000.

[13] S. Grivet-Talocia and F. Canavero, "Weak boundary treatment for high-order transient analysis of MTL's," in *Proc. IEEE Int. Symp. EMC 2000*, Washington, DC, pp. 409–414.

[14] ——, "Strictly stable high order schemes for transient analysis of MTL's," in *Proc. EMC Eur. 2000, IV Eur.Symp. Electromagnetic Compatibility*, Brugge, Belgium, Sept. 11–15, 2000, pp. 71–76.

[15] S. Grivet-Talocia, "Adaptive transient solution of nonuniform multiconductor transmission lines using wavelets," *IEEE Trans. Antennas Propagat.*, vol. 48, pp. 1563–1573, Oct. 2000.

[16] B. Gustafsson, H. O. Kreiss, and J. Oliger, *Time Dependent Problems and Difference Methods*. New York: Wiley, 1995.

[17] K. S. Kunz and R. J. Luebbers, *The Finite Difference Time Domain Method for Electromagnetics*. Boca Raton, FL: CRC , 1993.

[18] I. S. Stievano and I. A. Maio, "Behavioral models of digital IC ports from measured transient waveforms," in *Proc. IEEE 9th Topical Meeting on Electrical Performance of Electronic Packaging (EPEP'00)*, Scottsdale, AZ, Oct. 23–25, 2000, pp. 211–214.

[19] N. S. Nahman and D. R. Holt, "Transient analysis of coaxial cables using the skin effect approximation $A + B\sqrt{s}$," *IEEE Trans. Circuit Theory*, vol. CT–19, pp. 443–451, Sept. 1972.

[20] A. Orlandi and C. R. Paul, "FDTD analysis of lossy, multiconductor transmission lines terminated in arbitrary loads," *IEEE Trans. Electromagn. Compat.*, vol. 38, pp. 388–398, Aug. 1996.

[21] J. A. Roden, C. R. Paul, W. T. Smith, and S. D. Gedney, "Finite-difference, time-domain analysis of lossy transmission lines," *IEEE Trans. Electromagn. Compat.*, vol. 38, pp. 15–24, Feb. 1996.

[22] C. R. Paul, *Analysis of Multiconductor Transmission Lines*. New York: Wiley , 1994.

[23] ——, "Decoupling the multiconductor transmission line equations," *IEEE Trans. Microwave Theory Tech.*, vol. 44, pp. 1429–1440, Aug. 1996.

[24] A. Ralston and P. Rabinowitz, *A First Course in Numerical Analysis*. London, U.K.: McGraw-Hill, 1982.

[25] J. A. Roden, C. R. Paul, W. T. Smith, and S. D. Gedney, "Finite-difference, time-domain analysis of lossy transmission lines," *IEEE Trans. Electromagn. Compat.*, vol. 38, pp. 15–24, Feb. 1996.

[26] A. Ruehli, Ed., *Circuit Analysis, Simulation, and Design*. New York: Elsevier, 1987, pt. 1.

[27] B. Strand, "Summation by parts for finite difference approximations for d/dx," *J. Comput. Phys.*, vol. 110, pp. 47–67, Jan. 1994.

[28] ——, "Numerical studies of hyperbolic IBVP with high-order difference operators satisfying a summation by parts rule," *Appl. Numer. Math.*, vol. 26, no. 4, pp. 497–521, 1998.

[29] A. Taflove, *Computational Electrodynamics: The Finite-Difference Time-Domain Method*. Boston, MA: Artech House, 1995.

[30] C. F. Van Loan, "The ubiquitous Kronecker product," *J. Comput. Appl. Math.*, vol. 123, no. 1–2, pp. 85–100, 2000.

[31] J. Vlach and K. Singhal, *Computer Methods for Circuit Analysis and Design*. Norwell, MA: Kluwer, 1993.

S. Grivet-Talocia received the Laurea (*summa cum laude*) and the Ph.D. degrees in electronic engineering from the Politechnic of Turin, Turin, Italy.

From 1994 to 1996, he was at NASA/Goddard Space Flight Center, Greenbelt, MD, where he worked on applications of fractal geometry and wavelet transform to the analysis and processing of geophysical time series. In 1996, he joined the Electromagnetic Compatibility group in the Electronics Department of the Politechnic of Turin, working as a Researcher and Assistant Professor. His current research interests are in numerical modeling of transmission-line structures, applications of wavelets to computational electromagnetics, and reduced-order modeling of lumped and distributed structures.

From 1999 to 2000, he served as Associate Editor for the IEEE TRANSACTIONS ON ELECTROMAGNETIC COMPATIBILITY.

Flavio G. Canavero received the Laurea degree in electronic engineering from the Polytechnic University of Turin, Italy, in 1977, and the Ph.D. degree from the Georgia Institute of Technology, Atlanta, USA, in 1986.

Currently he is a Professor of Circuit Theory and Electromagnetic Compatibility with the Department of Electronics of the Polytechnic of Turin.

His research interests are in the field of Electromagnetic Compatibility, where he works on line modeling and digital integrated circuits characterization for signal integrity, field coupling to multiwire lines, and statistical methods in EMC. He is the Managing Editor of IEEE TRANSACTIONS ON ELECTROMAGNETIC COMPATIBILITY and Chair of the Workshop on Signal Propagation on Interconnects (SPI).